Supporting Information

Zhang et al. 10.1073/pnas.1713832115

Core Shape of $-1/2$ Defect

Elastic constant ratio κ also alters the core shape of $-1/2$ defects. As shown in Fig. S1, the defect cores adopt different shapes at different κ, despite the director fields looking similar. When $K_{33} = K_{11}$, the core periphery is a circle, whereas, when $K_{33} \neq K_{11}$, the core exhibits a triangular-like shape. The orientation of such a "triangle" depends on κ. The underlying reason is again related to the splay/bend distribution near $-1/2$ defect. It is not surprising that the defect core is circular when splay and bend are symmetric. If splay and bend are unequal, the threefold symmetry of the splay/bend energy leads to the triangular-like core shape. When $K_{33} < K_{11}$, bend is cheap, and thus the isosurface of elastic energy advances along the high bend region (blue), resulting in the triangle's orientation pointing to the left. When $K_{33} > K_{11}$, splay is cheap, and therefore the isosurface of elastic energy advances along the high splay region (red), leading to the triangle's orientation pointing to the right.

Extracting κ from Defect Morphology

We measure the dependence of κ with distance r from the defect core shown in Fig. S2*A*. The defects analyzed are the same as shown in Fig. 2. The range of r is chosen to avoid regions very close to the defect core, which is $\sim$2 μm and very far from the core where the director field is distorted by the surrounding defects. We find that κ increases with the filament length and also shows a radial dependence, as shown in Fig. S2*B*. The radial dependence is minimal for l = 1.5 μm where the $\theta(\phi)$ plot is linear, a result which is in accordance with the observations made in ref. 1. To extract the values of κ, we take its average close to the maxima where it remains constant over a relatively large distance (solid symbols in Fig. S2*B*). In all three cases, this distance was smaller than the mean interdefect separation, which is at least 30 μm.

Morphology of $+1/2$ Defect for Long Actin Filaments

Here we extract κ for the case when the actin filament length is comparable to its persistence length. We perform an experiment without adding capping protein so that the filaments grow to a length of $\sim$10 μm and analyze the shape of a typical $+1/2$ defect. The results in Fig. S3 show that κ = 0.28, smaller than κ = 2.13 for l = 2 μm.

Simple Theory on the Elasticities of Microtubule Doped Actin LC

The total elastic energy of the microtubule–actin composite consists of the Frank elastic energy of the nematic LC and the elastic energy of the microtubules. Elastic beam theory is adopted to describe the latter energy. The energy reads

$$F = \int_V dV \left\{ \frac{1}{2}K_{11}(\nabla\cdot\mathbf{n})^2 + \frac{1}{2}K_{22}(\mathbf{n}\cdot\nabla\times\mathbf{n})^2 + \frac{1}{2}K_{33}(\mathbf{n}\times(\nabla\times\mathbf{n}))^2 \right\} + N\int_{l_0} dy \frac{1}{2}EI\left(\frac{\partial^2 w}{\partial y^2}\right)^2, \quad \textbf{[S1]}$$

where N is the number of microtubule filaments, and l_0 is their average contour length; w is the displacement (see Fig. S5 for illustration). We assume that microtubules are aligning with the local director field $\mathbf{n}$; thus $w(y) = \int_0^y \tan\theta(y')dy'$. Taking the derivative to the above equation, one has $\frac{\partial w}{\partial y} = \tan\theta$. At weak bending limit, $\theta \sim 0$, therefore $\frac{\partial w}{\partial y} = \tan\theta \simeq \sin\theta$. We further have $\frac{\partial^2 w}{\partial y^2} = \cos\theta\frac{\partial\theta}{\partial y}$, thus

$$\frac{1}{2}EI\left(\frac{\partial^2 w}{\partial y^2}\right)^2 = \frac{1}{2}EI\cos^2\theta\left(\frac{\partial\theta}{\partial y}\right)^2 = \frac{1}{2}EI(\mathbf{n}\times(\nabla\times\mathbf{n}))^2.$$

The last equation is based on writing $\mathbf{n}$ as $\mathbf{n} = (\sin\theta(y), \cos\theta(y), 0)$. One has $\mathbf{n}\times(\nabla\times\mathbf{n}) = (-\cos^2\theta\frac{\partial\theta}{\partial y}, \sin\theta\cos\theta\frac{\partial\theta}{\partial y}, 0)$. Therefore, Eq. **S1** is rewritten as

$$F = \int_V dV \left\{ \frac{1}{2}K_{11}(\nabla\cdot\mathbf{n})^2 + \frac{1}{2}K_{22}(\mathbf{n}\cdot\nabla\times\mathbf{n})^2 + \frac{1}{2}(K_{33} + cl_0EI)(\mathbf{n}\times(\nabla\times\mathbf{n}))^2 \right\}, \quad \textbf{[S2]}$$

with c the number density of microtubules, i.e., $c = N/V$. The modified bend constant becomes $K'_{33} = K_{33} + cl_0EI$. For a 2D system, one has to consider the film thickness δ_z, $K'_{33} = K_{33} + cl_0EI/\delta_z$, in which $c = N/A$ with A denoting the film area.

Defect Annihilation

In Fig. S6, we show the trajectories of a $\pm 1/2$ defect pair during an annihilation event. We consider two defect configurations, with and without hydrodynamic effects. Elasticity is varied for each case. Without hydrodynamics, the relative velocity is dependent on κ and how the defects are organized: When the defect line is perpendicular (parallel) to the far field, the $+1/2$ defect moves faster (slower) than the $-1/2$ defect with $K_{33} < K_{11}$. As a special case when $K_{11} = K_{33}$, the two defects move at the same speed, consistent with previous calculations (2). When hydrodynamic effect is included, the $+1/2$ defect is more accelerated than the $-1/2$ defect, again consistent with reported experimental and simulation results (2, 3). The order of velocity anisotropy with respect to κ is kept if hydrodynamic effect is considered: Hydrodynamic flow does not change the qualitative behavior of the elasticity dependence of the defect velocity, and it only modifies the quantitative dependence. We point out that a pure elastic situation is not artificial. If the 2D system is strongly confined, the long-range hydrodynamic flow can be suppressed, and the defect dynamics can be approximated at a no-hydrodynamics assumption (4). Therefore, one should expect that, at a strong confinement system, it is possible that the $-1/2$ defect moves faster than the $+1/2$ defect in an annihilation event.

1. Zhou S, et al. (2014) Elasticity, viscosity, and orientational fluctuations of a lyotropic chromonic nematic liquid crystal disodium cromoglycate. *Soft Matter* 10:6571–6581.
2. Tóth G, Denniston C, Yeomans JM (2002) Hydrodynamics of topological defects in nematic liquid crystals. *Phys Rev Lett* 88:105504.
3. Yanagimachi T, Yasuzuka S, Yamamura Y, Saito K (2012) Cell gap dependence of nematic backflow around annihilating disclination pair. *J Phys Soc Jpn* 81:074603.
4. Brugués J, Ignés-Mullol J, Casademunt J, Sagueés F (2008) Probing elastic anisotropy from defect dynamics in Langumuir monolayers. *Phys Rev Lett* 100:037801.

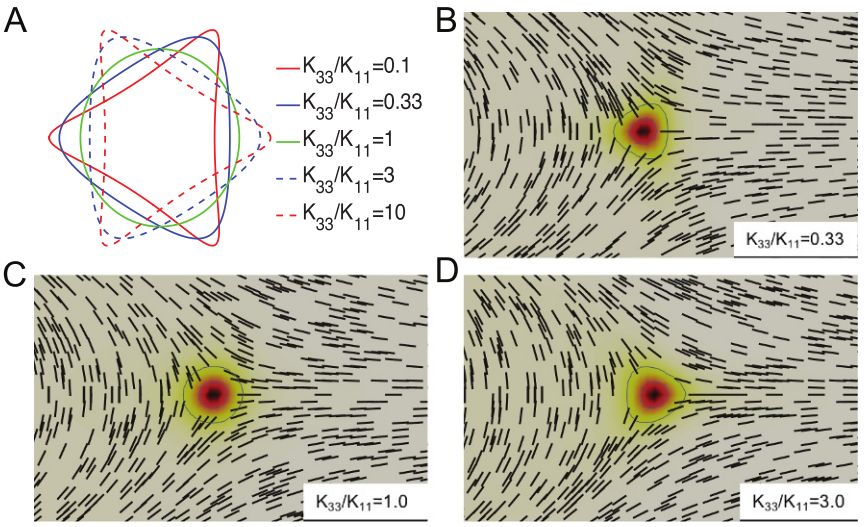

Fig. S1. Core shape of topological defects. (*A*) Defect core shape calculated from the minimization of Frank–Oseen elastic energy. (*B–D*) **Q**-tensor simulation results of the $-1/2$ defects with various K_{33}/K_{11}. Isosurfaces of the scalar order parameter are shown in black curves surrounding the defect core.

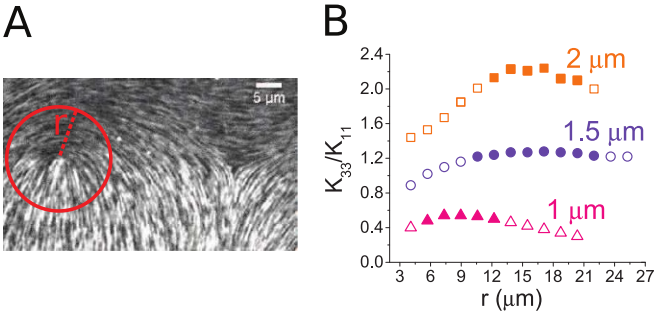

Fig. S2. Radial dependence of K_{33}/K_{11}. (*A*) A schematic description of the defect morphology where we plot the angle $\theta(r)$ against the polar coordinate ϕ. (*B*) The elasticity ratio, K_{33}/K_{11}, plotted as a function of the radial distance, r, from the defect core for three actin filament lengths corresponding to the images shown in Fig. 2*B*. Solid symbols represent the points over which K_{33}/K_{11} is averaged to extract the numbers presented in Fig. 2*C*.

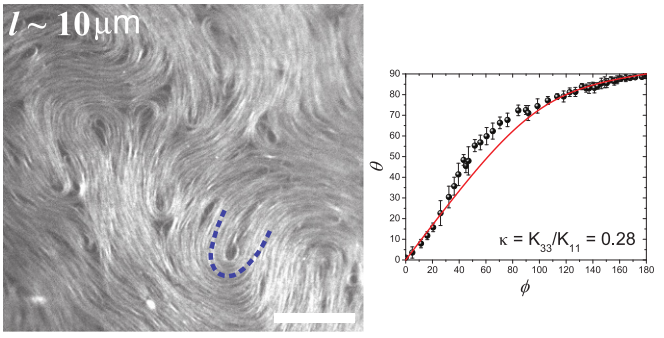

Fig. S3. The +1/2 defect shape for long actin filaments. Fluorescent image of LC formed by long actin filaments. A typical +1/2 defect is highlighted by a blue dashed line, and the graph shows the corresponding $\theta(\phi)$ plot for that defect. (Scale bar, 20 μm.)

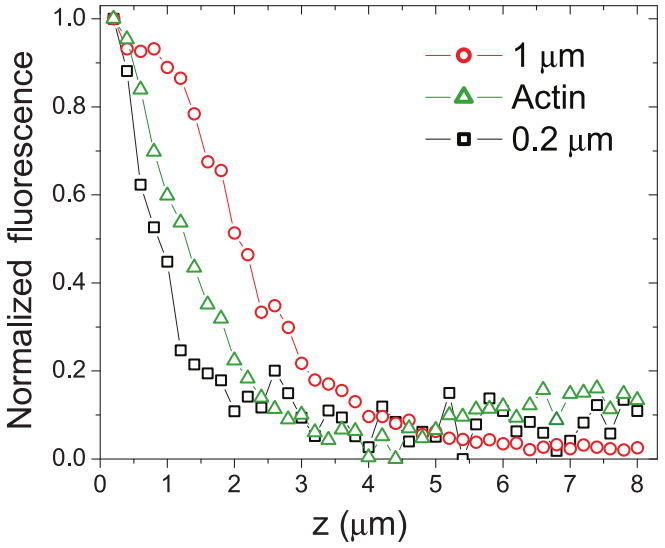

Fig. S4. Actin film thickness estimate. Green triangles show the normalized fluorescence intensity vs. distance from the oil–water interface (*z*) as acquired from a confocal *z* stack. Comparison with the beads of diameter 1 μm and 0.2 μm stuck on a glass surface (red circles and black squares, respectively) suggests that the actin film is ∼300 nm thick.

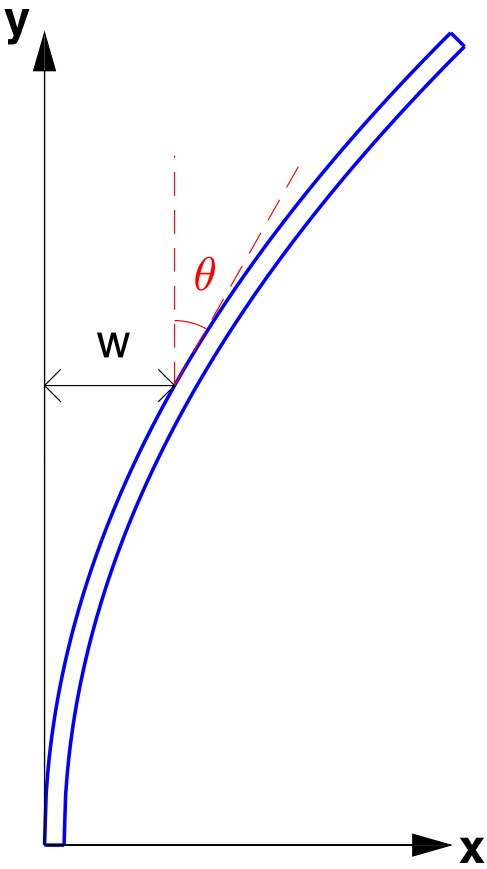

Fig. S5. Elastic beam. The schematic of the elastic beam theory in which *w* and θ are defined.

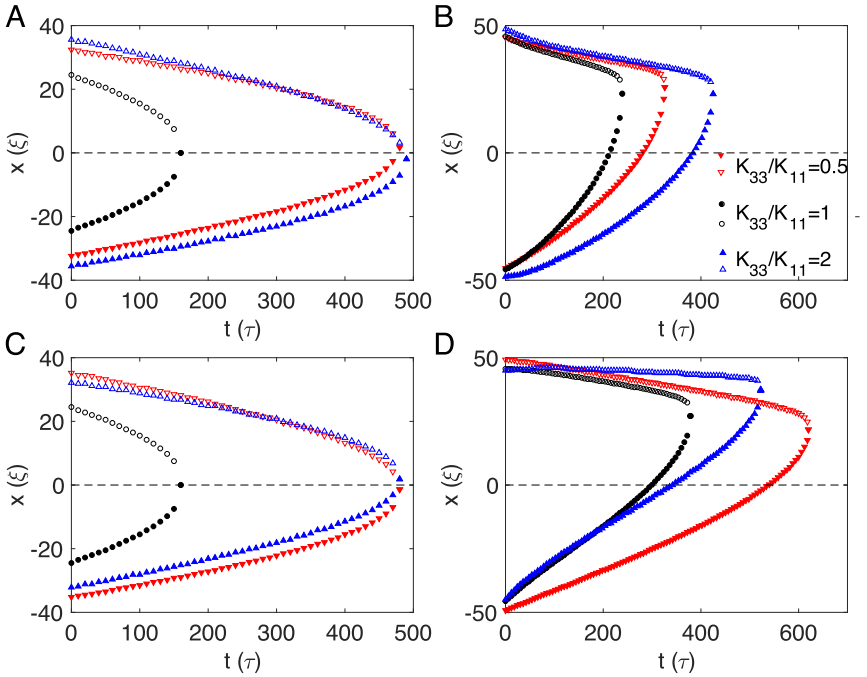

Fig. S6. Simulations of defect annihilation dynamics. Defect positions are plotted against time; 0 is where they meet if they move in the same speed. The filled symbols depict $+1/2$ defects, and open symbols represent $-1/2$ defects. (*A*) Perpendicular case without hydrodynamic effects. (*B*) Perpendicular case with hydrodynamic effects. (*C*) Parallel case without hydrodynamic effects. (*D*) Parallel case with hydrodynamic effects.

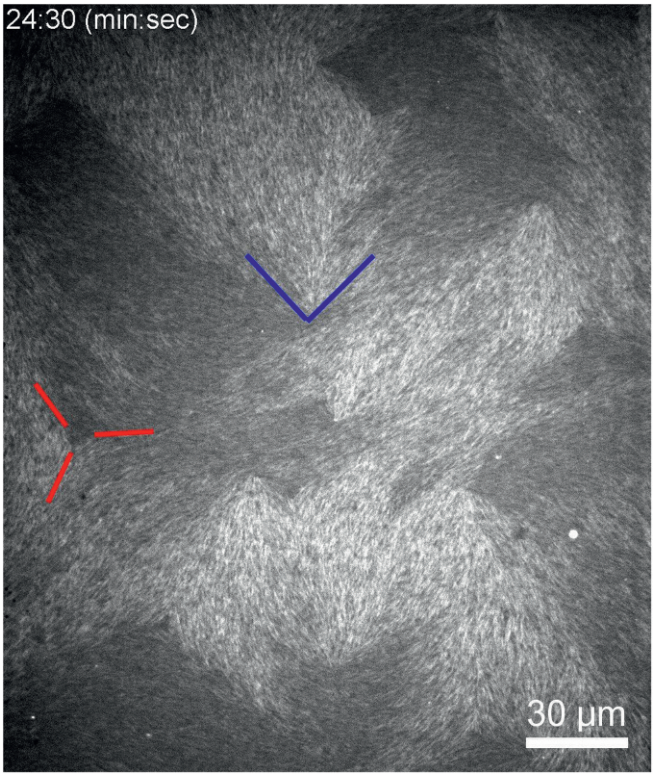

Movie S1. Crowding of actin filaments on an oil–water interface forming a 2D nematic LC. Red and blue lines in the end of the movie represent typical $+1/2$ and $-1/2$ defects. The data correspond to an average filament length of 2 μm.

Movie S1

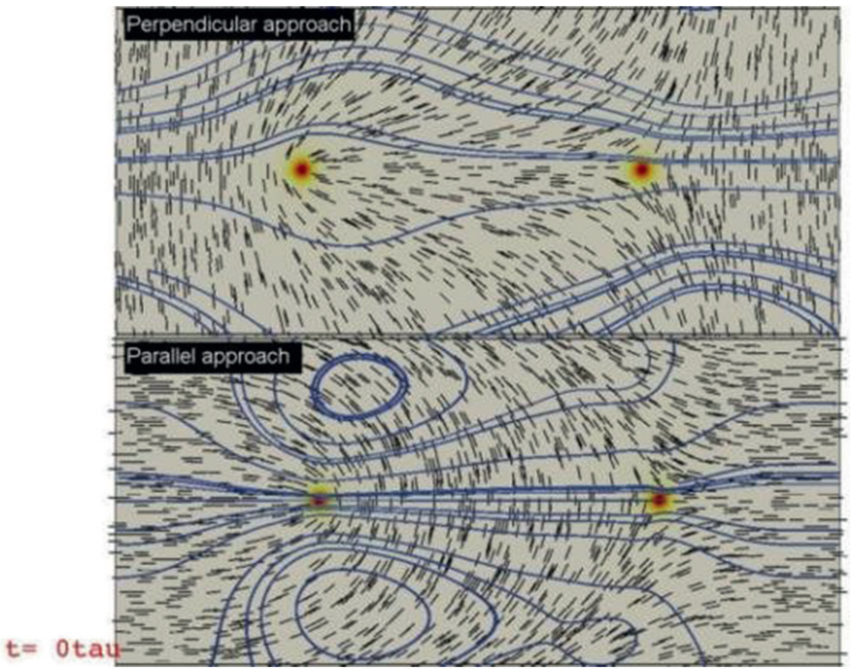

Movie S2. Simulation of two scenarios of the annihilation event of the $\pm 1/2$ defect. (*Upper*) Defect line perpendicular to the nematic far field. (*Lower*) Defect line parallel to the nematic far field. Short black lines represent the director field, and blue curves are streamlines. In the zoom-in frames, red arrows are the velocity vectors. In the parallel case, defects take a longer time to annihilate. (Time unit, tau = 0.8 s.)

Movie S2

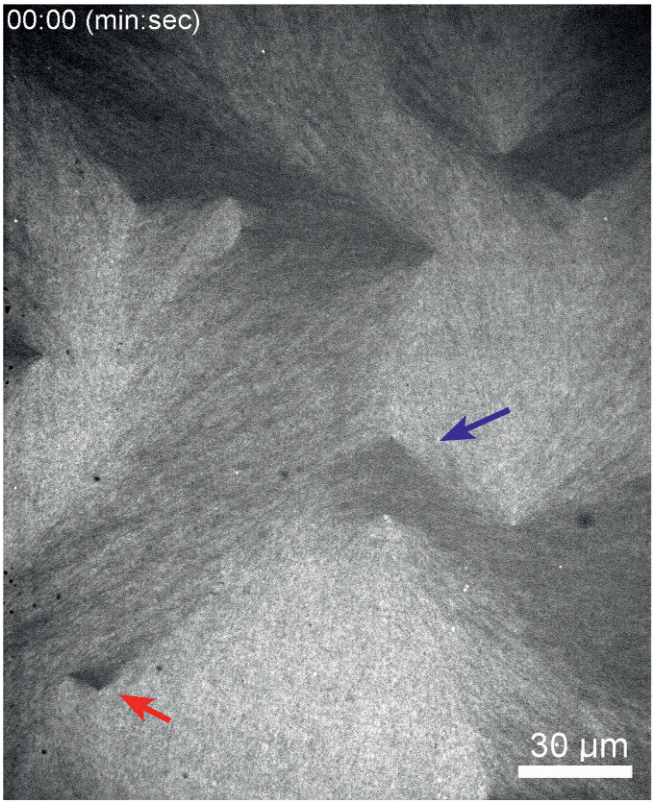

Movie S3. Experimental observations of the two scenarios of defect annihilation with perpendicular and parallel approach highlighted by red and blue arrows, respectively. The data correspond to an average filament length of 2 μm.

Movie S3

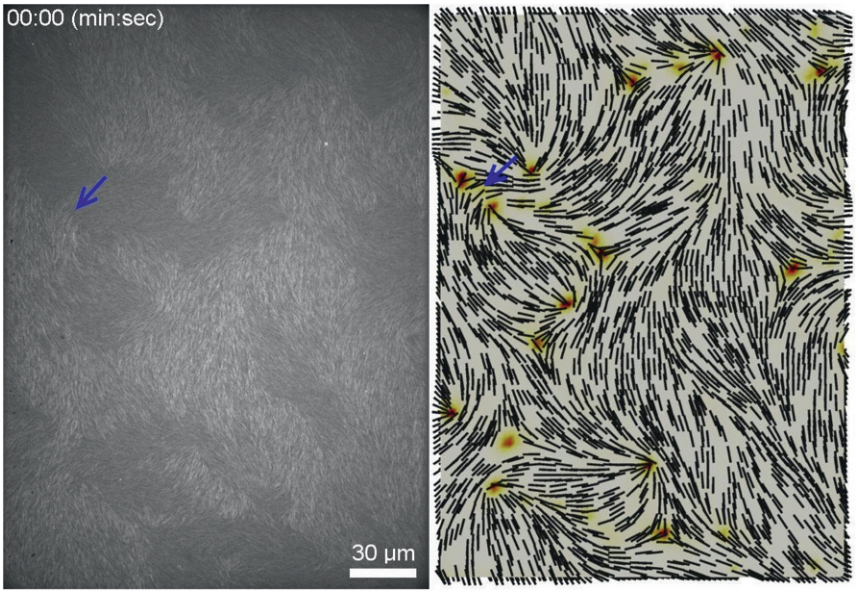

Movie S4. Weather map: comparison of defect evolution in experiment and simulation. The blue and red arrows represent defect annihilations with far-field parallel and perpendicular, respectively. The experimental data correspond to an average filament length of 2 μm.

Movie S4